



# 1 **Multiscale Roughness Influence on Conservative Solute Transport in Self-affine**

## 2 **Fractures**

3 *Zhi Dou<sup>a,b</sup>, Brent Sleep<sup>b</sup>, Hongbin Zhan<sup>c</sup>, Zhifang Zhou<sup>a</sup>, and Jinguo Wang<sup>a</sup>*

4 <sup>a</sup> *School of Earth Sciences and Engineering, Hohai University, Nanjing, 210098 China*

5 <sup>b</sup> *Department of Civil Engineering, University of Toronto, 35 St. George Street, Toronto, ON M5S 1A4, Canada*

6 <sup>c</sup> *Department of Geology and Geophysics, Texas A&M University, College Station, TX 77843-3115, USA*

7 *Correspondence to: Zhi Dou ([douz@hhu.edu.cn](mailto:douz@hhu.edu.cn)); Brent Sleep ([Sleep@ecf.utoronto.ca](mailto:Sleep@ecf.utoronto.ca))*

8

### 9 **Key Points:**

- 10 • Investigating the influence of large and small-scale roughness on transport of a conservative solute through a self-  
11 affine fracture.
- 12 • Removing small-scale secondary roughness delayed the arrival time and shortened the tail of BTCs.
- 13 • Small-scale secondary roughness decreased MIM mobile domain fraction and increased mass exchange rate between  
14 immobile and mobile domains.



15 **Abstract:** In this article, the influence of multiscale roughness on transport of a conservative solute through a self-affine  
16 fracture was investigated. The fracture roughness was decomposed into two different scales (i.e., a small-scale stationary  
17 secondary roughness superimposed on a large-scale non-stationary primary roughness) by a wavelet analysis technique.  
18 The fluid flow in the single fracture was characterized by Forchheimer's law and exhibited nonlinear flow features such  
19 as eddies and tortuous streamlines. The results indicated that the small-scale secondary roughness was primarily  
20 responsible for the nonlinear flow features. Numerical simulations of asymptotic conservative solute transport showed  
21 non-Fickian transport characteristics (i.e., early arrivals and long tails) in breakthrough curves (BTCs) and in residence  
22 time distributions (RTDs) with and without consideration of the secondary roughness. Analysis of multiscale BTCs and  
23 RTDs showed that the small-scale secondary roughness played a significant role in enhancing the non-Fickian transport  
24 characteristics. Removing small-scale secondary roughness delayed the arrival time and shortened the tail. The peak  
25 concentrations in BTCs decreased as the secondary roughness was removed, implying that the secondary roughness  
26 could also enhance the solute dilution. Fitting the one-dimensional (1D) Fickian advection-dispersion equation (ADE) to  
27 the numerical BTCs resulted in considerable errors that decreased with the small-scale secondary roughness being  
28 removed. The 1D mobile-immobile model (MIM) provided a better fit to the numerical BTCs and inclusion of the small-  
29 scale secondary roughness in numerical simulations resulted in a decreasing MIM mobile domain fraction and an  
30 increasing mass exchange rate between immobile and mobile domains.

31 **Keywords:** simulation; fracture; self-affine; multiscale roughness; non-Fickian transport; mobile-immobile model.



## 32 **1. Introduction**

33 Characterizing the transport behavior of a conservative solute through a heterogeneous geological formation is crucial  
34 for many environmental and hydrogeological problems such as enhanced oil recovery, geothermal energy development,  
35 remediation of contaminated groundwater, and carbon storage. The heterogeneity of geological formations is ubiquitous  
36 and occurs at all scales in subsurface. Even in a single fracture, the roughness of fracture walls plays an important role in  
37 the transport behavior of a conservative solute at different scales, with solute transport varying from Fickian to non-  
38 Fickian (anomalous) regimes (Dentz et al., 2004). Improving the fundamental understanding and predictability of  
39 conservative solute transport behavior through single fractures at various scales is important for analyzing anomalous  
40 hydrogeological phenomena (Berkowitz, 2002;Dentz et al., 2011).

41 The fluid flow behavior, as a background information, is of importance in analyzing the conservative solute transport  
42 behavior in rough fractures. To this end, the fracture roughness effect on the fluid flow has attracted much attention in the  
43 last several decades (Zimmerman and Bodvarsson, 1996;Brush and Thomson, 2003;Brown, 1987). Based on the ideal  
44 smooth parallel plate model, the classical cubic law is widely used to simplify fluid flow in single rough fractures.  
45 However, many theoretical and experimental studies reported that the classical cubic law was valid when the flow was  
46 linear (or the inertial effect was negligible) and may result in non-negligible errors when the fracture walls were rough.

47 To improve the performance of the cubic law, several studies (Zimmerman et al., 1991;Oron and Berkowitz, 1998)  
48 noticed the influence of the local aperture and developed the well-known local cubic law that is able to explicitly consider



49 the spatial variability in aperture. Renshaw (1995) considered a correction factor based on fracture roughness to modify  
50 the cubic law and showed that the modified cubic law was capable of describing a nonlinear relationship between the  
51 fracture hydraulic and the mechanical apertures. Konzuk and Kueper (2004) evaluated various modifications of the cubic  
52 law and found that even at the typical groundwater flow rate with the Reynolds number less than 1 ( $Re < 1$ ), the flow rate  
53 in single rough fractures was over-predicted at least 1.75 times by the local cubic law. A recent work reported by Wang et  
54 al. (2015) showed that the accuracy of the local cubic law could be improved by consideration of the local tortuosity and  
55 roughness. However, important characterizations of the nonlinear flow through rough fractures (i.e., eddies) was  
56 neglected by Wang *et al.* (2015).

57 Several studies (Drazer et al., 2004; Jin et al., 2017; Kang et al., 2016) revealed that both flow and transport behaviors  
58 are sensitive not only to roughness but also to the scale of roughness. According to the roughness definition by the  
59 International Society of Rock Mechanics (ISRM) (Barton, 1978), the original fracture roughness can be also considered  
60 as a two-scale combination (i.e., a small-scale unevenness superimposed on a large-scale waviness). The large-scale  
61 waviness represents the primary waviness geometry (i.e., non-stationary primary roughness) and the small-scale  
62 unevenness represents the secondary waviness geometry (i.e., stationary secondary roughness). With this conceptual  
63 understanding, Zou et al. (2015) and Wang et al. (2016) investigated the importance of secondary roughness on the  
64 nonlinear flow behavior in the two-dimensional (2D) and three-dimensional (3D) rough fractures, respectively. Since the  
65 transport of a conservative solute is intrinsically coupled with fluid flow, our current interest is to further investigate



66 conservative solute transport behavior for two different scales of fracture roughness by using the roughness definition of  
67 ISRM.

68 Fick's law has been widely used to describe solute transport for many decades (Fetter, 2000; Bear, 1972). The Fickian  
69 transport model (i.e., advection-dispersion equation or ADE) always yields well-behaved breakthrough curves (BTCs).  
70 However, a large body of evidence indicates that the anomalous (non-Fickian) BTCs associated with the early arrival and  
71 long tails is ubiquitous in geological formations. This phenomenon is caused by the well-known non-Fickian transport  
72 behavior, which is present even in a single fracture due to the fracture roughness (Thompson, 1991; Tsang and Tsang,  
73 1989; Boutt et al., 2006). Cardenas et al. (2007) used the 2D Navier-Stokes (N-S) equation to simulate the solute transport  
74 in a single rough fracture and showed that eddies observed at regions with relatively large apertures led to a power-law  
75 tail in BTCs. Zheng et al. (2009) investigated the influence of aperture heterogeneity and anisotropy on solute transport  
76 and showed that the dominant dispersion regime varied with statistical properties of aperture field such as mean, standard  
77 deviation, and anisotropic ratio. Wang and Cardenas (2014) reported a detailed numerical investigation on the  
78 relationship between the magnitude of fracture heterogeneity and non-Fickian transport behavior. Fiori and Becker (2015)  
79 used a purely advective model to analyze the long tails of BTCs in a variable-aperture fracture based on the statistical  
80 parameters in transmissivity field. Recently, Wang and Cardenas (2017) quantified the dependence of non-Fickian  
81 transport on the fracture roughness with consideration of increasing fracture length scales. Without consideration of  
82 roughness scales, Dou et al. (2018a) quantified the uniformity of concentration distribution based on the concept of



83 dilution index (Kitanidis, 1994) and their results showed roughness-induced eddies could provide resistance for the solute  
84 transport.

85 To explain non-Fickian transport, several transport models were developed such as the continuous time random walk  
86 (CTRW) (Berkowitz et al., 2006), the fractional advection-dispersion equation (FADE) (Benson, 1998), the mobile-  
87 immobile model (MIM) (Van Genuchten and Wierenga, 1976), the equivalent-stratified medium (Nowamooz et al.,  
88 2013), and the multi-rate mass transfer model (Haggerty, 2013). A detailed description and comparison of these transport  
89 models can be found in several recent studies (Neuman and Tartakovsky, 2009;Gao et al., 2009). Fitting non-Fickian  
90 BTCs to different transport models can accurately estimate the transport parameters and quantify the characterization of  
91 the non-Fickian transport. The ADE has been inversely applied to estimate solute transport parameters in fractures for  
92 many decades. However, the ADE model was proven to be incapable of explaining non-Fickian transport (i.e., scale-  
93 dependent spreading, early arrival and long tails in BTCs) and consequently fitting non-Fickian BTCs using the ADE  
94 model showed persistent errors (Becker and Shapiro, 2003;Bijeljic and Blunt, 2006;Briggs et al., 2014;Dou and Zhou,  
95 2014;Jiménez - Hornero et al., 2005).

96 Alternatively, some other non-Fickian models have been applied to fit the non-Fickian BTCs obtained in physical and  
97 numerical experiments carried out in single fractures. Bauget and Fourar (2008) experimentally investigated non-Fickian  
98 transport in a single rough fracture. Their results showed that the ADE model was unable to capture the long tail of BTCs  
99 while the CTRW model was robust enough to model the non-Fickian transport due to the fracture roughness. Qian et al.



100 (2011b) studied the capacity of the MIM model for solute transport in a single fracture under non-Darcian flow  
101 conditions. Their results showed that the MIM model captured both peak and tails in the BTCs better than the ADE  
102 model. Recently, Cherubini et al. (2014) compared the performance and reliability of the MIM model and the explicit  
103 network model (ENM) in a fracture network. Their results showed that although the ENM model better fitted BTCs  
104 observed in a fracture network than the MIM model, the latter remained valid as well. This could be attributable to the  
105 capability of the MIM model to intrinsically separate solute spreading into dispersion in the mobile region and mobile-  
106 immobile mass transfer (Gao et al., 2009; Qian et al., 2011a).

107 The goal of this study is to investigate the influence of roughness on conservative solute transport in self-affine  
108 fractures for two different scales of fracture roughness. Although Dou et al. (2018a) revealed that the roughness-induced  
109 eddies, which could be considered as an immobile region in the MIM model, provided resistance for the solute transport,  
110 the influence mechanism of the different scales of fracture roughness on the mass transfer between mobile and immobile  
111 regions was not investigated. Moreover, our previous work (Dou et al., 2018b) based on CTRW model had demonstrated  
112 the roughness scale dependence of the relationship between the longitudinal dispersion ( $D_L$ ) and Peclet number ( $Pe$ ), in  
113 which the method of decomposing the fracture roughness into different scales was capable of providing an effective path.  
114 Hence, we here focus on the differences in flow and solute transport at two different scales to provide a fundamental  
115 understanding of the influence of roughness and physical insight into the inherent mechanism of transport, especially the  
116 mass transfer between mobile and immobile regions, in single rough fractures. For this, we first generate self-affine  
117 fracture walls by the successive random additions (SRA) procedure and then decompose the roughness of the synthetic



118 fracture into a primary roughness (large-scale) and a secondary roughness (small-scale) by a wavelet analysis technique.  
119 The flow field and conservative solute transport in the original fracture and the primary fracture (without secondary  
120 roughness) are simulated by coupling the N-S equation and ADE. Fluid flow is analyzed by Forchheimer's law and BTCs  
121 are characterized by a proper inverse model (MIM model).

## 122 **2. Construction and Decomposition of a Self-affine Fracture**

### 123 **2.1 Construction of a Self-affine Fracture**

124 The surface of natural fractures typically follows a statistical self-affine distribution (Mandelbrot, 1983). Thus, to  
125 construct a synthetic fracture, a self-affine fracture wall should be generated first. A 2D self-affine fracture wall height,  
126  $Z(x)$ , satisfies,

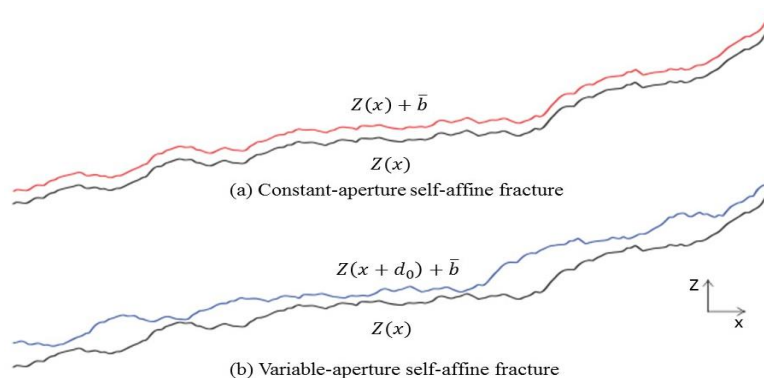
$$127 \lambda^H Z(x) = Z(\lambda x) \quad (1)$$

128 where  $H$  indicates the roughness magnitude or the so-called Hurst exponent, varying from 0 to 1 (dimensionless) and  $\lambda$  is  
129 a scaling factor (dimensionless).  $Z(x)$  can be thought of as a function of an independent spatial or temporal variable  $x$   
130 ( $L$ ). Here the successive random additions (SRA) method (Voss, 1988) is applied to generate self-affine walls. A more  
131 detailed application for generating the self-affine wall by the SRA method can be found in our previous work (Dou et al.,  
132 2013). It should be noted that to generate the self-affine wall by using the SRA method, the desired Hurst exponent must



133 be selected. Previous studies (Boffa et al., 1998; Schmittbuhl et al., 1993) on self-affinity of fractured rock showed that  
 134 the  $H = 0.8$  could be as a characteristic Hurst exponent of self-affine fractures.

135 In this study, we use  $H = 0.8$  as a characteristic Hurst exponent of self-affine fractures and used two different ways to  
 136 obtain the synthetic self-affine fracture with the generated self-affine walls. First, the generated self-affine wall  $Z(x)$  is  
 137 considered as the lower fracture wall and the upper fracture wall is translated a vertical distance  $\bar{b}$  without the relative  
 138 lateral displacement of  $d_0$ . As a result, the local aperture in the constructed self-affine fracture is constant and equal to  $\bar{b}$   
 139 but the fracture wall is rough and self-affine (i.e. constant-aperture self-affine fracture), as shown in Figure 1 (a).  
 140 Alternatively, the two fracture walls can have a relative lateral displacement of  $d_0$ , which results in the fact that the two  
 141 fracture walls do not overlap (i.e. variable-aperture self-affine fracture), as shown in Figure 1 (b). Thus, the local aperture  
 142  $b(x)$  varies along the longitudinal direction,  $b(x) = Z(x + d_0) - Z(x) + \bar{b}$ . In this study, we consider a variable-aperture  
 143 self-affine fracture with  $H=0.8$  and a total fracture length of 0.2 m as an example to illustrate the transport feature.



144



145 Figure 1. The construction process of synthetic self-affine fracture with  $H=0.8$  and a total fracture length of 0.2 m.

## 146 2.2 Decomposition of the Self-Affine Fracture

147 The self-affine wall can be considered as signal profiles due to the local change of geometries at different scales.  
148 Here,  $f(s)$  is defined as the fracture wall profile. Analogous to the signal profiles, the  $f$  function representing the  
149 variation of the wall height is similar to the dependent variable in the frequency domain, while  $s$  representing the  
150 variation of the distance along in-plane direction of fracture is similar to the dependent variable in the time domain.  
151 Previous studies (Wang et al., 2016; Zou et al., 2015) have shown that the wavelet analysis method is more suitable than  
152 other mathematical methods (i.e., image analysis and Fourier transform) for decomposing the self-affine roughness into  
153 primary (non-stationary) and secondary (stationary) roughness components. The non-stationary primary roughness  
154 represents larger scale undulations or waviness with the lower frequency, while the stationary secondary roughness  
155 represents the higher frequency variability. The wavelet transform of the self-affine fracture profile is given as,

$$156 \quad W(a, \tilde{s}) = \int_{-\infty}^{+\infty} f(\tau) \psi_{a,s}(s) ds \quad (2)$$

157 where  $\tilde{s}$  represents the horizontal distance,  $a$  can be considered as a scaling parameter and represents the frequency of the  
158 height profile of the original wall, and  $\psi_{a,s}(s)$  is the so-called mother wavelet function expressed as,

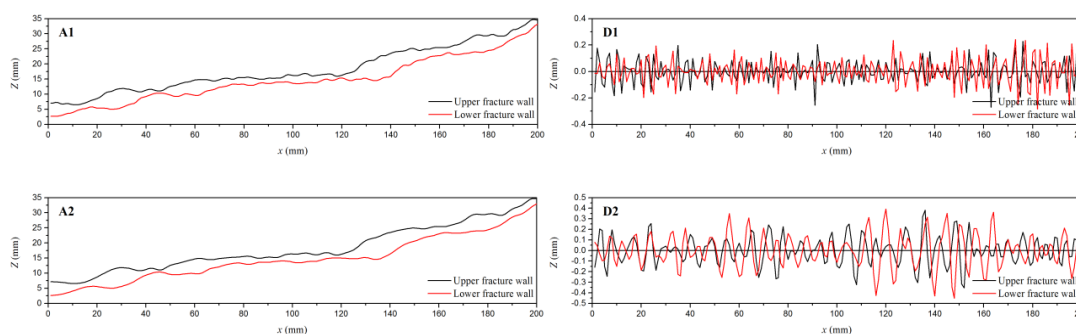
$$159 \quad \psi_{a,s}(s) = a^{-\frac{1}{2}} \psi\left(\frac{s-\tilde{s}}{a}\right) \quad (3)$$



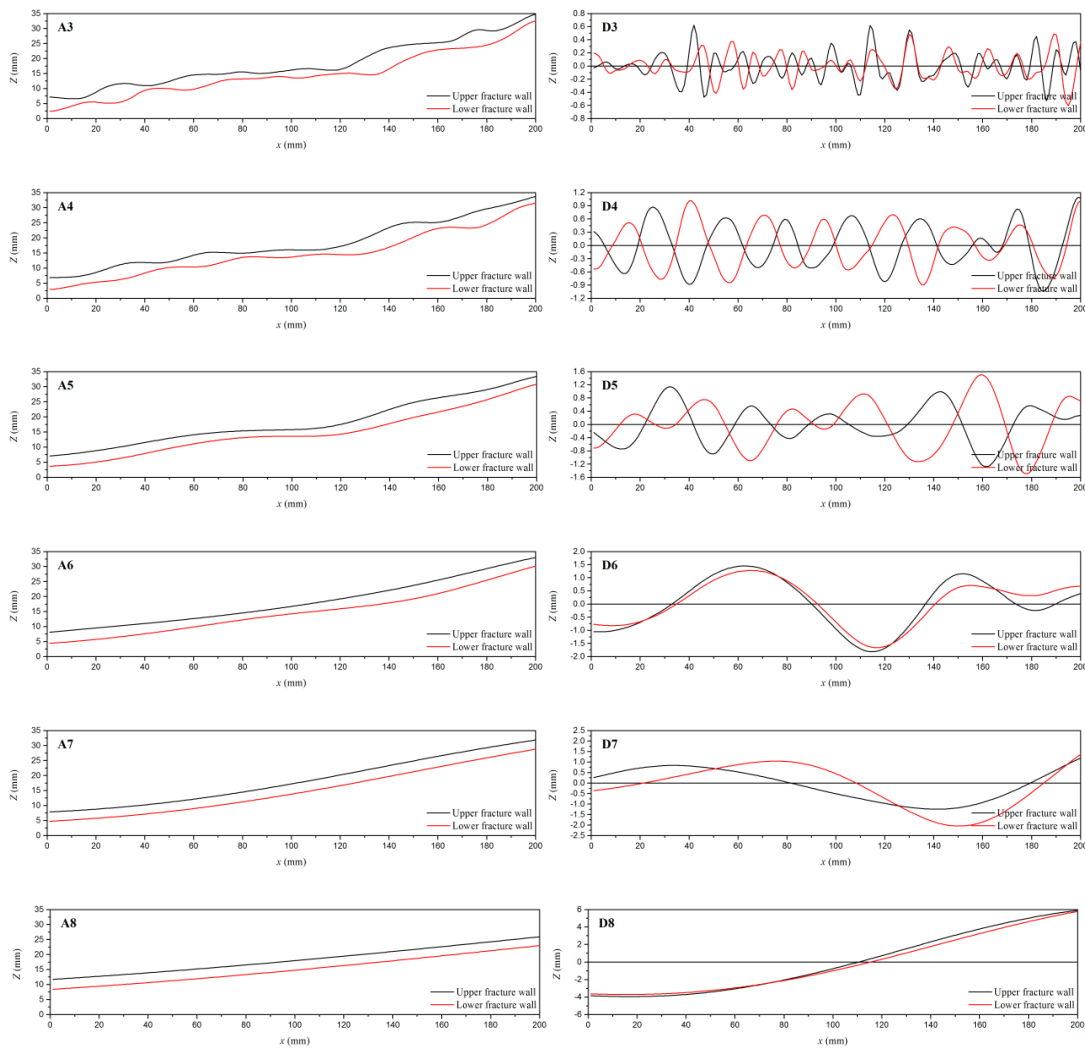
160 An appropriate mother wavelet function is important to decompose the roughness component of the self-affine fracture  
161 profile.

162 In this study, we used the Daubechies Wavelet as the mother wavelet. The process of roughness decomposition is  
163 realized by Mallat's pyramidal algorithm in a level-by-level procedure (Mallat, 1989). In each level, the self-affine  
164 fracture wall is decomposed into low and high frequency components. The low frequency component is defined as an  
165 approximate wall and represented the dominant geometrical formation of waviness or unevenness. The high frequency  
166 component is defined as a detailed wall and represented the small-scale waviness or unevenness. As shown in Figure 2,  
167 the decomposition of reconstruction of the original rough fracture walls are implemented at 8 levels, noted by A1-A8 and  
168 D1-D8, respectively. For each level, the approximation walls,  $A_i$ , represent the primary waviness (non-stationary primary  
169 roughness) and the detailed walls,  $D_i$ , represent the small-scale unevenness (stationary secondary roughness).

170



171



172

173

174

175

176

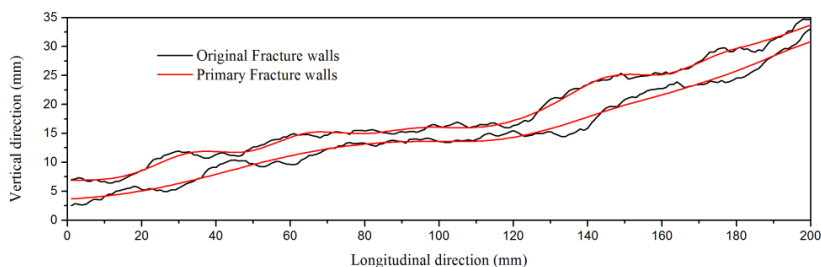
177



178 Figure 2. 8 levels decomposition of the roughness for the self-affine fracture with  $H=0.8$ . A1-A8 and D1-D8 represent the  
179 approximate walls and the detailed walls, respectively.

180 During the process of roughness decomposition, it is crucial to determine an appropriate cut-off level for separating  
181 roughness into the non-stationary primary roughness and the secondary roughness, where the non-stationary primary  
182 roughness should be dominant for the geometric property, while the secondary roughness could be treated as a Gaussian  
183 white noise process. Here, we use the quantitative criterion proposed by (Zou et al., 2015). In Zou's quantitative criterion,  
184 the cut-off level is determined by analyzing the variance of the primary roughness, and locating where the variance of the  
185 primary roughness changes significantly, while the secondary roughness could be considered as a Gaussian white noise  
186 with a mean value close to zero.

187 Based on Zou's quantitative criterion, the cut-off levels for the fracture walls in Fig.2 are level 4 and level 5 for top  
188 and bottom fracture walls, respectively. Consequently, the level 4 and level 5 approximation walls are considered as the  
189 primary roughnesses for top and bottom fracture walls, respectively. The secondary roughnesses of top and bottom  
190 fracture walls are determined by summing the level 1-4 and level 1-5 detailed walls, respectively. Hereafter, the  
191 undecomposed fracture is denoted as the original fracture, while the decomposed fracture (with secondary roughness  
192 removed) is denoted as the primary fracture.



193

194 Figure 3. Comparison of original and primary fracture walls after the roughness decomposition. The primary fracture  
 195 walls only contain the non-stationary primary roughness of the original roughness where the stationary secondary  
 196 roughness is removed.

197

Table 1. The statistical properties of original and primary fractures

Fracture	$\bar{b}$ (mm)	$\sigma$ (mm)	COV
Original	3.3871	1.6502	0.4872
Primary	3.3701	0.9839	0.2920

198

199 Figure 3 shows the original fracture wall and the primary fracture wall after the roughness decomposition. It can be  
 200 seen that the primary fracture wall without the secondary roughness is smoother than the original fracture wall. The



201 statistical properties of the original and primary fractures are listed in Table 1. The decomposition of fracture roughness  
202 has little influence on the average aperture but leads to a decreasing coefficient of variation (COV).

### 203 **3. Direct Numerical Simulation: Fluid Flow and Conservative Solute Transport**

#### 204 **3.1 Fluid flow**

205 The fluid flow in single fractures is solved directly by the continuity equation (Eq. 4) and the N-S equation (Eq. 5)  
206 under isothermal, incompressible, Newtonian, and steady-state flow conditions,

$$207 \quad \nabla \cdot \mathbf{u} = 0 \quad (4)$$

$$208 \quad -\nabla p = \rho(\mathbf{u} \cdot \nabla \mathbf{u}) - \nabla(\mu \nabla \mathbf{u}) \quad (5)$$

209 where  $\mathbf{u} = [u, w]$  denotes the 2D velocity vector with components of  $u$  and  $w$ , respectively ( $\text{LT}^{-1}$ ),  $\rho$  represents the  
210 density of fluid ( $\text{ML}^{-3}$ ),  $\mu$  is defined as the dynamic viscosity of fluid ( $\text{ML}^{-1}\text{T}^{-1}$ ), and  $p$  is the fluid pressure  
211 ( $\text{ML}^{-1}\text{T}^{-2}$ ). The standard water properties at  $20^\circ\text{C}$  (i.e.,  $\rho=998.2 \text{ kg/m}^3$  and  $\mu=1.002 \times 10^{-3} \text{ Pa}\cdot\text{s}$ ) was used in this study.  
212 The non-slip boundary conditions are applied for the fracture walls. As background flow, the steady-state flow is induced  
213 by a given pressure gradient over the entire fracture. The COMSOL Multiphysics package (COMSOL Inc., Burlington,  
214 MA, USA), a Galerkin finite-element software package, serves as a numerical solver for Eqs. (4) and (5). The calculating  
215 domain for the fracture is discretized into 148,000 triangular elements (TE). A superfine mesh size (0.00015 mm) is  
216 imposed near the fracture walls to capture the non-slip boundaries. The number of TE was determined by the mesh



217 independence analysis. Under the same pressure gradient (i.e.,  $-\nabla p=200$  Pa/m), the steady-state flow rate changes about  
218 0.5% (from  $1.215 \times 10^{-4}$  m<sup>3</sup>/s to  $1.221 \times 10^{-4}$  m<sup>3</sup>/s) as the number of TE increases by about 100% (from 148,000 to  
219 295,000), indicating that the 148,000 TE for the given fracture are sufficient to provide stable and accurate numerical  
220 results. The dimensionless Reynolds number ( $Re$ ) is given as ,

$$221 \quad Re = \frac{\rho Q}{\mu W} \quad (6)$$

222 where  $W$  denotes the width of fracture in the out of plane direction ( $W=1$  m for the 2D problem) and  $Q$  represents the  
223 flow rate (L<sup>3</sup>T<sup>-1</sup>). We consider four different flow fields in both original and primary fractures where the  $Re$  value varies  
224 from 3.1 to 71.8.

### 225 3.2 Conservative solute transport

226 The conservative solute transport simulation is first attempted using the advection-diffusion equation,

$$227 \quad \frac{\partial c}{\partial t} = -\nabla(\mathbf{u}c) + D_m \nabla^2 c \quad (7)$$

228 where  $t$  represents time (T),  $c$  denotes the conservative solute concentration (ML<sup>-3</sup>),  $D_m$  is defined as the diffusion  
229 (L<sup>2</sup>T<sup>-1</sup>), and the 2D velocity tensor  $\mathbf{u}$  is determined by the numerical solution of Eqs. (4) and (5). In this study, we  
230 consider two different injection conditions for the solute transport simulation.



231 The first injection condition is simulated with the Dirac delta function. We assume that the concentrations of initial  
 232 instantaneous sources follow a sole function of the longitudinal coordinate  $x_L^*$ . Thus, the initial condition for Eq. (7) is  
 233 specified as,

$$234 \quad c(\mathbf{x}, t = 0) = c_0(x_L^*) \quad (8)$$

235 where  $c_0(x)$  is given by

$$236 \quad c_0(x) = \begin{cases} \delta(t) \frac{m_0}{b(x) \Delta L} & \text{if } x_L^* < x < x_L^* + \Delta L \\ 0 & \text{otherwise} \end{cases} \quad (9)$$

237 where  $\delta(t)$  represents the Dirac delta function for the time variable,  $m_0$  is the mass of injected solute (M),  $b(x)$  is the  
 238 local aperture (L) and  $\Delta L$  is the width of injected solute (L).  $\Delta L$  is constant in all the simulations and  $\Delta L/L = 0.001$ ,  
 239 where  $L$  is the fracture length. The inlet and outlet boundary conditions are specified as,

$$240 \quad c(0, t) = 0 \quad t \geq 0 \quad (10)$$

$$241 \quad \partial c(L, t) / \partial n = 0 \quad t \geq 0 \quad (11)$$

242 where  $n$  is the direction normal to the outlet boundary.

243 The second injection condition tested is continuous solute injection at the inlet boundary. This is the so-called step  
 244 injection condition. To do this, the inlet boundary condition in Eq. (10) becomes a Dirichlet boundary condition with the  
 245 assumption of step injection concentration with  $c_0 = 1$  and is given by



246 
$$c(0, t) = c_0 = 1 \quad t > 0 \quad (12)$$

247 where 1 in Eq. (12) represents a specified unit concentration.

248 The ratio of effluent solute mass to fluid mass is expressed as the BTCs,,

249 
$$c_f = \frac{\int_0^b ucdz}{\int_0^b u dz} \quad (13)$$

250 and the normalized BTCs and time are respectively,

251 
$$c' = c_f/c_0 \quad (14)$$

252 
$$t' = Qt/AL \quad (15)$$

253 Where  $A$  is the area of the 2D fracture ( $L^2$ ),  $t'$  is the dimensionless time or number of pore volume (PV), and  $c'$  is the  
254 dimensionless concentration. The mesh used in solute transport simulation is the same as the fluid flow simulation. The  
255 numerical dispersion can be negligible depending on sensitivity analysis of mesh size and time step.

256 In this study, we define the Peclet number ( $Pe$ ),  $Pe = \tau_D/\tau_u = \bar{u}\bar{b}/D_m$ , as the ratio of the characteristic diffusive  
257 time ( $\tau_D = \bar{b}^2/D_m$ ) to the characteristic advective time ( $\tau_u = \bar{b}/\bar{u}$ ). To investigate the independent influence of  
258 multiscale roughness, rather than the combined influence of multiscale roughness and fracture length scale on the  
259 transport, we consider the case of solute transport at the potential asymptotic time scale. In such a condition, anomalous  
260 early arrival and long tails in BTCs, which is the classical non-Fickian behavior, is caused by the influence of roughness  
261 rather than the pre-asymptotic transport of a conservative solute due to the limitation of the fracture length scale. Based  
262 on the equivalent 2D ideal model (Wang et al., 2012), we calculate the potential asymptotic time (T) for the self-affine  
263 fractures. Following Taylor's seminal work (Aris, 1956), the potential critical time (T) is given as



264 
$$T_t = \bar{b}^2 / 4D_m \quad (16)$$

265 At times larger than  $T_t$ , the transverse diffusion gradient eventually leads to complete cross-sectional homogenization of  
266 the solute distribution. For a given fracture, the critical mean advective velocity ( $LS^{-1}$ ) can be obtained by

267 
$$U_a = L/T_t = 4D_m L / \bar{b}^2 \quad (17)$$

268 whereas the corresponding critical advective time (T) is

269 
$$T_a = \bar{b} / U_a = \bar{b}^3 / 4D_m L \quad (18)$$

270 Depending on the definition of  $Pe$ , the Peclet number corresponding to the critical advective time, denoted as  $Pe_a$ , for  
271 asymptotic solute transport is obtained as,

272 
$$Pe_a = \tau_d / T_a = 4L / \bar{b} \quad (19)$$

273 It can be seen from Eq.(19) that  $Pe_a$  is only dependent on the geometry of fracture. In this study,  $Pe_a$  is equal to 237  
274 and the solute transport therefore is simulated under the conditions of  $Pe = 8.8, 81.7, 147.6,$  and  $205.8,$  respectively. This  
275 implies that all of simulated solute transport is asymptotic and the non-Fickian transport behavior could be considered as  
276 a result of the influence of roughness rather than the length of fracture.

## 277 **4. Inverse Model for Solute Transport**

### 278 **4.1 Fickian transport model**



279 Based on Fick's law, the advection-diffusion equation (Eq.(7)) can be transformed to ADE by replacing the velocity  
 280 vector  $\mathbf{u}$  by the average velocity  $\bar{u}$ . For the step injection condition, the corresponding analytical solution for the ADE  
 281 model is given by

$$282 \quad C(x, t) = \frac{C_0}{2} \left[ \operatorname{erfc} \left( \frac{x - \bar{u}t}{2\sqrt{D_f t}} \right) + \exp \left( \frac{\bar{u}x}{D_f} \right) \operatorname{erfc} \left( \frac{x + \bar{u}t}{2\sqrt{D_f t}} \right) \right] \quad (20)$$

283 where  $D_f$  is the fitted dispersion coefficient ( $L^2 T^{-1}$ ). For the Dirac delta injection condition, the corresponding analytical  
 284 solution for the ADE model is given by

$$285 \quad c(x, t) = \frac{m_0}{A} \frac{x}{\sqrt{4\pi D_f t}} \exp \left( -\frac{(x - \bar{u}t)^2}{4D_f t} \right) \quad (21)$$

## 286 4.2 MIM model

287 Unlike the Fickian model, the single-rate MIM model describe the Fickian transport in the mobile domain and  
 288 diffusion-driven mass exchange between the mobile and immobile domains. For the conservative solute transport, the  
 289 MIM model is given as,

$$290 \quad \theta_m \frac{\partial c_m}{\partial t} = \theta_m D_{f,m} \frac{\partial^2 c_m}{\partial x^2} - \bar{u} \theta_m \frac{\partial c_m}{\partial x} - \alpha (c_m - c_{im}) \quad (22)$$

$$291 \quad \theta_{im} \frac{\partial c_{im}}{\partial t} = \alpha (c_m - c_{im}) \quad (23)$$



292 where  $c_m$  and  $c_{im}$  are defined as the solute concentrations in the mobile and immobile domains, respectively;  $\theta_m$  and  $\theta_{im}$   
293 represent the water contents in the mobile and immobile domains, respectively, and the sum of  $\theta_m$  and  $\theta_{im}$  is equal to  
294 one for a saturated 2D fracture;  $D_{f,m}$  represents the dispersion coefficient and  $\alpha$  is the mass transfer rate between the  
295 mobile and immobile domains ( $T^{-1}$ ). A dimensionless  $\beta = \theta_m / (\theta_{im} + \theta_m)$  is introduced as the mobile water fraction. It  
296 should be mentioned that our motivation to implement the MIM model is based on the assumption that the potential eddy-  
297 controlled domain can be considered as an immobile domain, rather than considering the fracture matrix as an immobile  
298 domain. Thus, we assume that the fracture matrix is impermeable.

### 299 4.3 Inverse parameter estimation from BTC

300 BTCs from numerical simulations can be used to estimate parameters used in the ADE or MIM model. The goodness-  
301 of-fitting was quantified by introducing a global error,  $E_i$ , which is given as,

$$302 \quad E_i = \sqrt{\sum_i^N (c_{fit,i} - c_{model})^2 / N} \quad (24)$$

303 where  $c_{fit,i}$  ( $i=1, 2, 3, \dots, N$ ) represents concentration in the fitted BTCs, and  $c_{model}$  is the BTCs from the numerical  
304 simulations,  $i$  refers to either the ADE or MIM model, and  $N$  represents the number of calculated data in BTCs. Global  
305 errors from the ADE and MIM models hereafter are denoted as  $E_{ADE}$  and  $E_{MIM}$ , respectively. Both of the velocity and  
306 dispersion coefficient are considered as the fitted parameters in the inverse parameter estimation with the ADE model.  
307 There are four initial input parameters,  $\beta$ ,  $\alpha$ ,  $\bar{u}_{f,MIM}$ , and  $D_{f,MIM}$  in the inverse parameters estimation with the MIM



308 model. Accurate initial guesses for fitted parameters would be beneficial to improve the convergence of the inverse model  
309 (Wang and Cardenas, 2014; Wang and Cardenas, 2015). The initial values of velocity  $\bar{u}_{f,MIM}$  and dispersion coefficient  
310  $D_{f,MIM}$  are set equal to the counterparts from the ADE model. The 1STOPT code and STANMOD V2.08 based on  
311 CXTFIT code (Toride et al., 1995) are employed for the inversion of the ADE and MIM models, respectively.

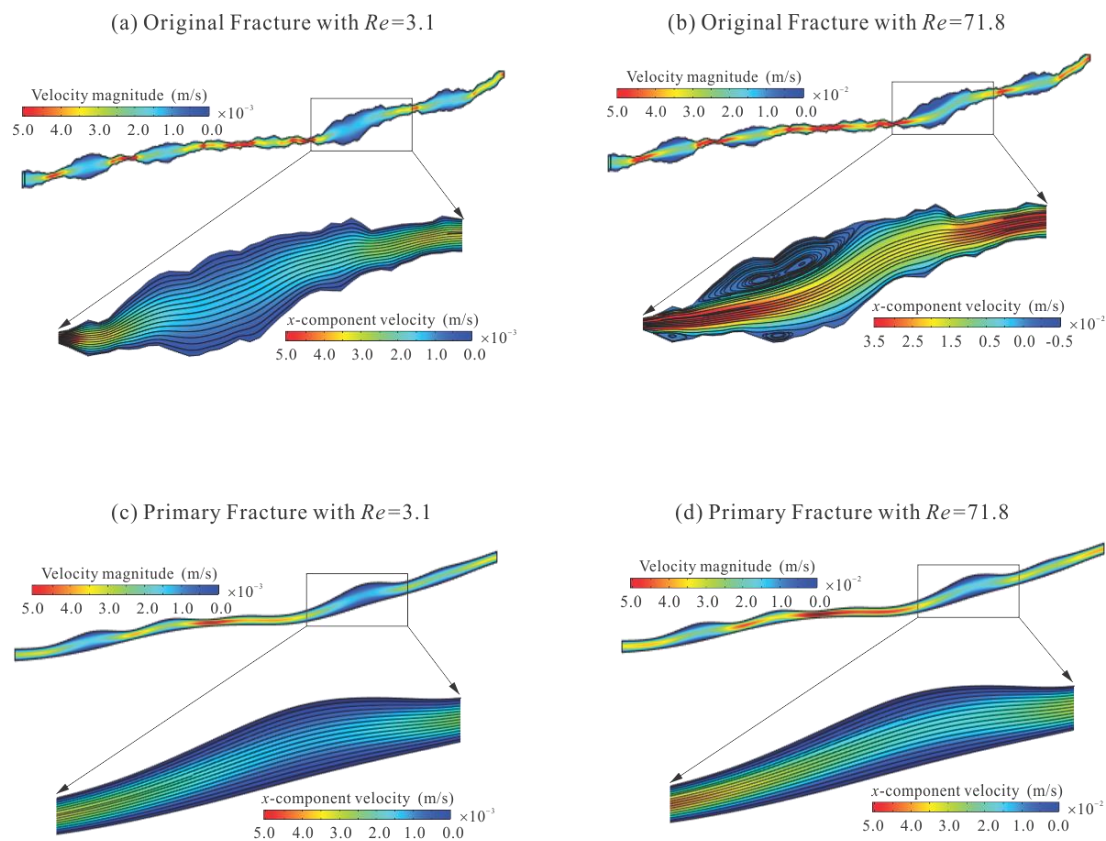
## 312 **5. Results and Discussion**

### 313 **5.1 Flow fields in original and primary fractures**

314 Flow at four different Reynolds numbers ( $Re=3.1, 28.5, 51.5, \text{ and } 71.8$ ) is simulated in the original and primary  
315 fractures. The flow fields in the original fracture and the primary fracture are denoted as OF#1-OF#4 and PF#1-PF#4,  
316 respectively. Without loss of generality, Figure 4 only illustrates the numerical results of OF#1, OF#4, PF#1, and PF#4  
317 where the influence of Reynolds numbers and roughness on the flow fields can be observed. Comparing Figs.4 (a) and 4  
318 (c), the flow velocity distribution is more heterogeneous in the original fracture than in the primary fracture. For both of  
319 the original and primary fractures, the relatively high local flow velocity is captured at small-aperture segments, while the  
320 relative low local flow velocity is observed at the abruptly changing large-aperture segments where the eddies form as the  
321 Reynolds number increases. The streamlines are smoother in the primary fracture than in the original fracture, suggesting  
322 that the tortuosity of the flow path is significantly influenced by the secondary roughness. As the Reynolds number  
323 increases, eddies form and develop at the abruptly changing large-aperture segments. As a result, the effective advection  
324 channel becomes narrow. Several previous works (Bouquain et al., 2012; Briggs et al., 2016; Qian et al., 2012) also



325 showed the similar results that increasing Reynolds number causes the growth of eddies. However, comparing Figs.4 (b)  
326 and 4 (d) for the primary fracture where the secondary roughness is not included, there are no visible eddies and the  
327 streamlines have the same patterns with cases at low Reynolds number (Fig. 4 (c)). This indicates that the secondary  
328 roughness is primarily responsible for the presence of eddies.



329



330 Figure 4. The non-uniform flow field in the self-affine fracture under the different Reynolds number. (a)-(b) and (c)-(d)  
331 represent the flow fields in the original and primary fractures with  $Re=3.1$  and  $71.8$ , respectively. The entire view of the  
332 fractures shows the velocity magnitude, while the corresponding enlarged segment shows the streamlines and  $x$ -  
333 component velocity distribution.

334 It should be mentioned that the presence of eddies cannot be used to determine if the flow regime is non-Darcian  
335 (nonlinear flow) or Darcian (linear flow). Since the discrepancies of solute transport behavior are captured under different  
336 flow regimes (Lee et al., 2015; Qian et al., 2011b; Qian et al., 2011a), it is necessary to determine when the flow regime is  
337 linear or nonlinear. For determining the flow regime in the simulations, Forchheimer's law (Jacob, 1972) is applied to  
338 determine the critical Reynolds number ( $Re_c$ ) that is proposed for characterizing the onset of flow transition to  
339 nonlinearity (Javadi et al., 2014). If the Reynolds number of fluid flow is less than  $Re_c$ , the fluid flow can be considered  
340 as linear. Otherwise, the fluid flow is the nonlinear. Forchheimer's law is:

$$341 \quad -\Delta p = aQ + bQ^2 \quad (25)$$

342 where  $a = 12\mu/W e_h^3$  ( $MT^{-1}L^{-5}$ ) and  $b = \beta\mu/W^2 e_h^2$  ( $ML^{-8}$ ) denote the linear and nonlinear coefficients, respectively,  
343 and  $\beta$  and  $e_h$  represent the Forchheimer coefficient and hydraulic aperture, respectively. When the inertial effect of fluid  
344 flow becomes negligible at low velocity, the nonlinear term (the second term on the right side of Eq. (25)) tends to zero  
345 and Forchheimer's law reduces to Darcy's law for linear flow.  $Re_c$  is given by

$$346 \quad Re_c = \frac{a\rho\alpha}{b\mu W(1-\alpha)} \quad (26)$$



347 where  $\alpha$  is a nonlinear effect factor denoted as the ratio of the nonlinear pressure drop to the overall pressure drop,  $\alpha =$   
348  $bQ^2/(aQ + bQ^2)$ . In this study, a critical value of  $\alpha = 5\%$  is used to quantify the transition of flow regimes from linear to  
349 nonlinear. This critical value for  $\alpha$  is consistent with previous studies (Wang et al., 2016; Zhou et al., 2015).

350 Table 2. Critical  $Re$  and best-fitted results from Forchheimer equation.

Fracture	$a$ ( $\text{kg} \cdot \text{s}^{-1} \cdot \text{m}^{-5}$ )	$b$ ( $\text{kg} \cdot \text{m}^{-8}$ )	$Re_c$
Original	$1.59 \times 10^6$	$8.30 \times 10^9$	10.1
Primary	$4.12 \times 10^5$	$5.22 \times 10^8$	41.4

351

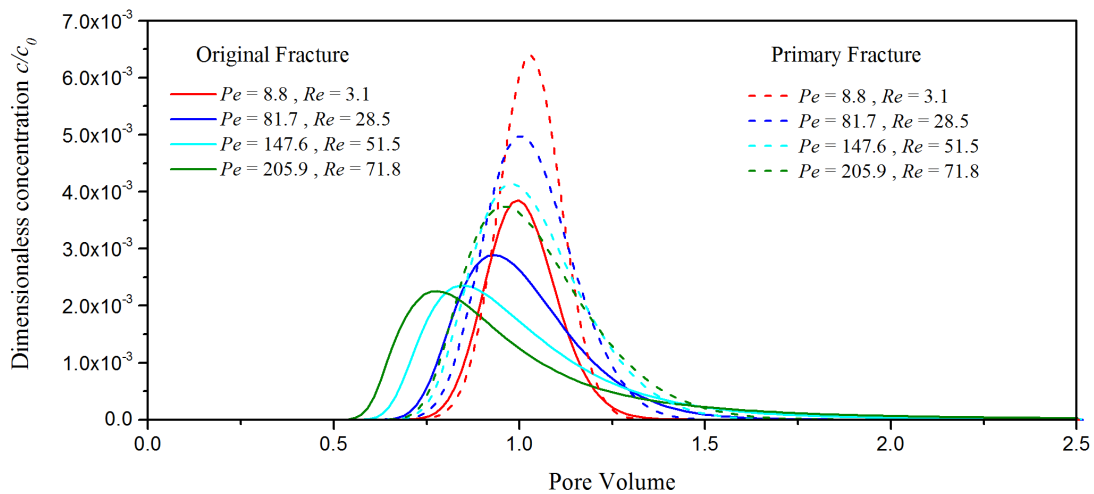
352 Table 2 lists the critical Reynolds number and the best-fitted results for the parameters ( $a$  and  $b$ ) in the Forchheimer  
353 equation for the original and primary fractures. The critical Reynolds number is smaller in the original fracture than in the  
354 primary fracture, which indicates that the secondary roughness significantly impacts the flow behavior. Thus, OF#1  
355 ( $Re=3.1$ ), PF#1 ( $Re=3.1$ ), and PF#2 ( $Re=28.5$ ) are in the linear flow regime, while the rest (OF#2-OF#4 and PF#3-PF#4)  
356 are in the non-linear flow regime.

## 357 5.2 BTCs and RTDs

358 To analyze the influence of secondary roughness on solute transport, the flux-weighted BTCs and RTDs are  
359 calculated from numerical simulations involving different Peclet numbers. Figure 5 shows the calculated BTCs in the  
360 original and primary fractures. In general, the apparent differences in BTCs between the original fracture and the primary  
361 fracture indicates that the secondary roughness plays a crucial role in the solute transport. The early arrival and long tail



362 as non-Fickian characteristics can be observed in all of the BTCs, indicating that the transport is non-Fickian. It should be  
363 noted that all of the Peclet numbers used in this study are less than the critical Peclet number for asymptotic solute  
364 transport. Thus, the fracture roughness rather than the length of the fracture leads to the non-Fickian transport behaviors.

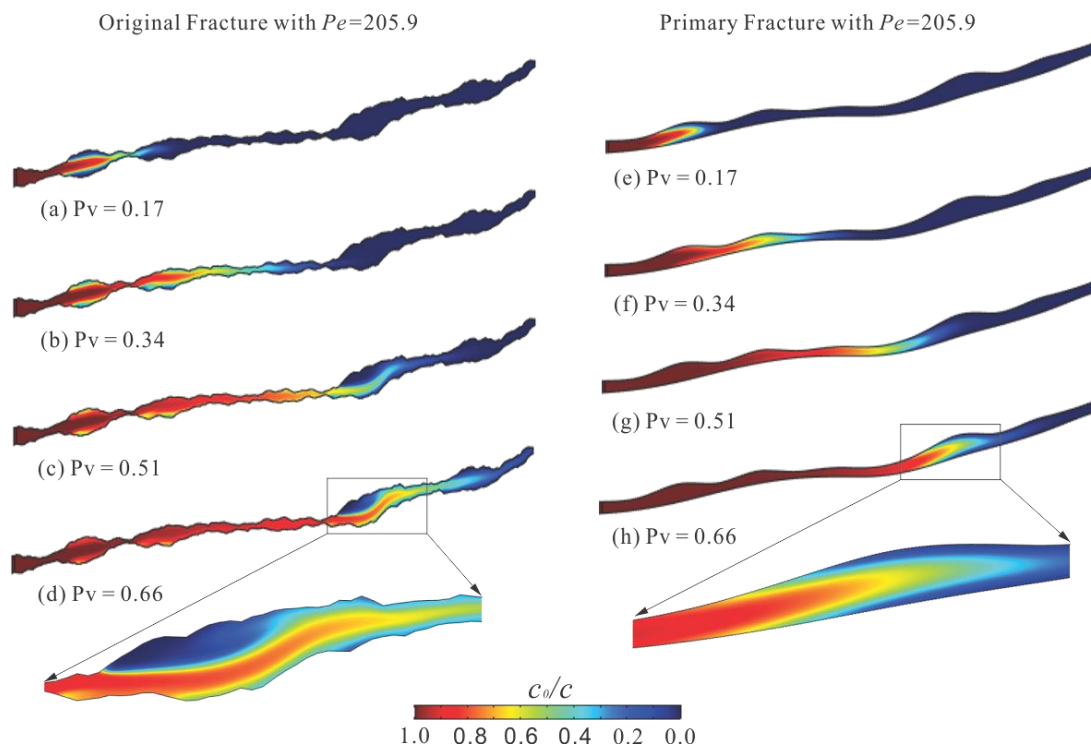


365  
366 Figure 5. The breakthrough curves under the different Peclet numbers at the outlets of the original fracture and the  
367 primary fracture.

368 In the original fracture (see Figure 5), the early arrival and long tail in the BTCs are enhanced as the Peclet number  
369 increases. Similar trends can be found in the primary fracture where the secondary roughness is excluded. However, the  
370 non-Fickian characteristics of BTCs are stronger in the original fracture than in the primary fracture, suggesting that the  
371 secondary roughness significantly enhances the non-Fickian characteristics of BTCs. This can be attributed to the fact



372 that the secondary roughness leads to enhanced nonlinear flow behavior. Another interesting finding is the peak  
373 concentration of BTCs. As the Peclet number and Reynolds number increase, the peak concentrations of the BTCs  
374 decrease. This trend is observed in both the original and primary fractures. This could be qualitatively explained from the  
375 view of the solute dilution (mixing) process in the sense that greater dilution leads to a lower peak concentration.  
376 Comparing BTCs in the original and primary fractures, the peak concentrations of BTCs are lower in the original fracture  
377 than in the primary fracture for the case with the same Peclet number. This implies that the solute dilution process is  
378 significantly enhanced by the secondary roughness. Although beyond the scope of the current study, it is worth noting  
379 that the magnitude of the solute dilution could be analyzed quantitatively using the concept of a scalar dissipation rate  
380 (Dreuzy et al., 2012; Le Borgne et al., 2010) and a statistical-entropy dilution index (Kitanidis, 1994).



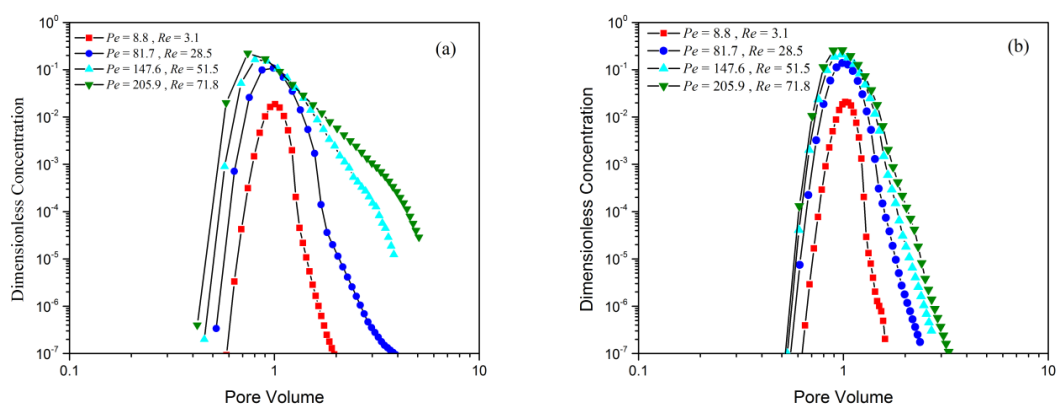
381

382 Figure 6. The spatial evolution of solute concentration distribution under  $Pe=205.9$  in the original fracture ((a)-(d)) and  
 383 the primary fracture ((e)-(h)), respectively.

384 Figure 6 shows the spatial evolution of solute concentration distribution for  $Pe=205.9$  in the original and primary  
 385 fractures. This evolution is found to be sensitive to the aperture. The solute is transported slower near the fracture walls  
 386 than in the middle clearly showing that there is an effective advection channel along the longitudinal direction for solute  
 387 transport. Comparing Figures 6 (a) and (b), the secondary roughness has an important influence on spatial evolution of



388 solute concentration distribution. The effective advection channel is narrower and more tortuous in the original fracture  
389 than in the primary fracture due to the fact that the growing eddy flow region is mainly due to the secondary roughness.



390

391 Figure 7. The RTDs under different Peclet numbers at the outlets of the original fracture (a) and the primary fracture (b),  
392 respectively.

393 RTDs were calculated for solute transport in both the original and primary fractures for characterizing the long tails of  
394 BTCs. Figs. 7 (a) and (b) show RTDs for different Peclet numbers in the original fracture and the primary fracture,  
395 respectively. The tails after the peak are apparent in the RTDs and follow a power-law drop (especially for the large  $Pe$ ).  
396 The degree of power-law drop increases as the Peclet number increases. Comparing RTDs in the original and primary  
397 fractures, removing the secondary roughness from the original fracture roughness leads to shortening tails. This could be  
398 attributed to the secondary roughness enhancing the nonlinear flow behavior.



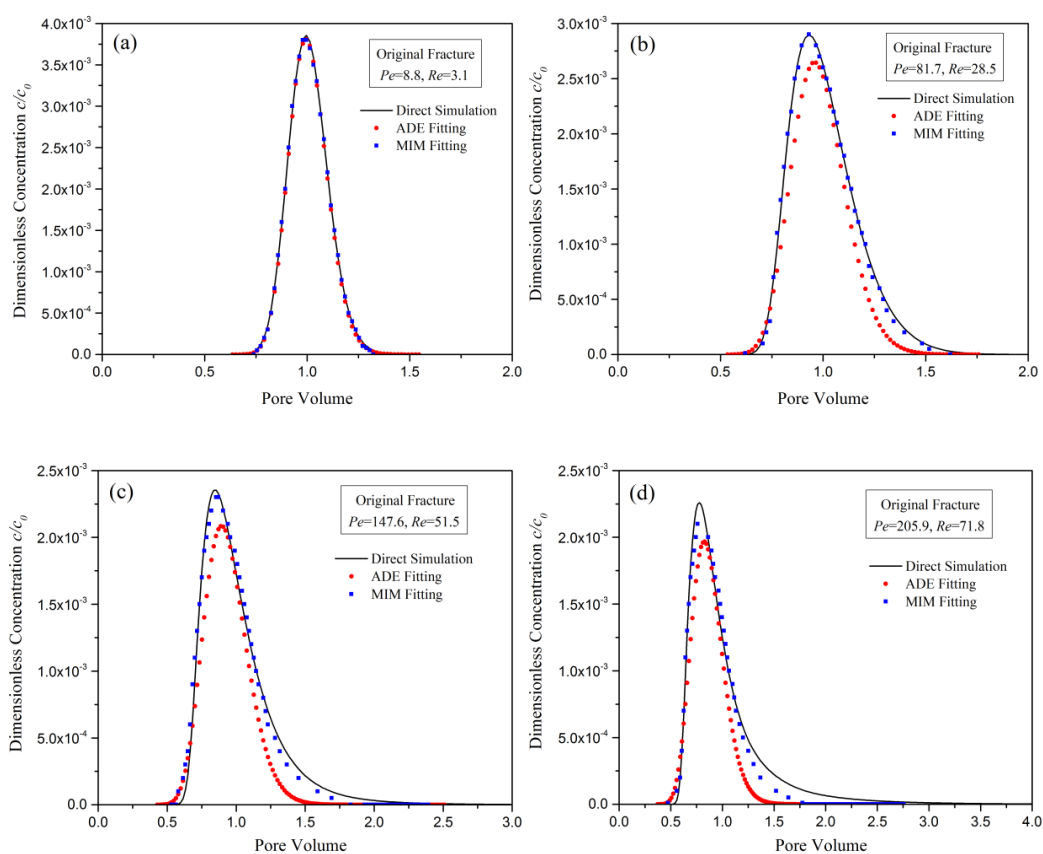
### 399 5.3 Inverse MIM and ADE models

400 To further investigate the fracture multiscale roughness influence on the transport behavior, the ADE and MIM model  
401 are used to fit all of the BTCs in the flow fields OF#1-OF#4 and PF#1-PF#4, respectively. Figure 8 shows the best-fitted  
402 results of BTCs using the ADE and MIM in the OF#1-OF#4. The ADE model is incapable of capturing the peak  
403 concentration and tails of BTCs. In contrast, the best-fitted results of BTCs from the MIM model do not exhibit a  
404 Gaussian-shaped distribution, showing that the MIM model is more capable than the ADE model for describing the  
405 roughness-induced non-Fickian characteristics of BTCs, especially the peak concentration and tail. This is also reflected  
406 by the coefficient of determination  $R^2$  and the global error ( $E_i$ ), as shown in Table 3.

407 Although the best-fitted results of BTCs are better from the MIM model than from the ADE model (Table 3), the  
408 results from both the ADE and MIM models tend to yield an increasing global error as the Peclet number and Reynolds  
409 number increase. This is reasonable because as the Reynolds number increases, the spreading and mixing of the solute  
410 would be significantly influenced by the enhanced non-linear flow behavior (i.e., eddies). In such a condition, the MIM  
411 model considering a single-rate exchange process between the immobile and mobile domains may be inadequate (Dentz  
412 and Berkowitz, 2003). Figures 8c and 8d show the deviations of MIM model to direct simulation results. As the Peclet  
413 number increases, the enhanced non-linear flow behavior could induce a distribution of eddies of evolving sizes. As a  
414 limitation of the single-rate exchange process in the MIM model, this evolution of the sizes of eddies with Peclet number  
415 for the same fracture may not be reflected by the MIM model, which has also been found in porous media (Dreuzy and  
416 Carrera, 2016). Our primary aim is not to analyze the validity of transport model but to emphasize the influence of the



417 fracture multiscale roughness on the transport mechanism. Comparing the results in Figures 8 and 9, the best-fitted results  
418 of the ADE and MIM models are better for the primary fracture than for the original fracture, which reflects the impact of  
419 secondary roughness on non-Fickian behavior and deviation from the ADE and MIM models.

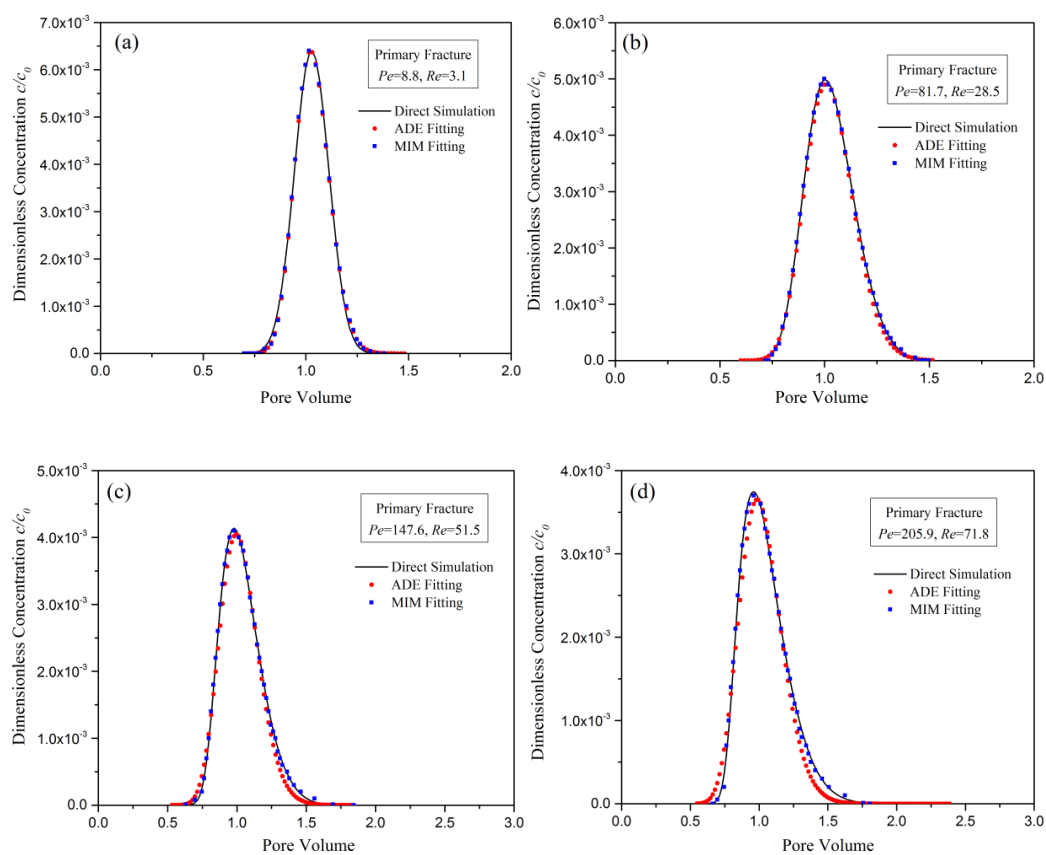


420

421



422 Figure 8. Best-fitted results of BTCs at different Peclet number and Reynolds number using the ADE and MIM models in  
423 the original fracture.



424

425

426 Figure 9. Best-fitted results of BTCs at different Peclet number and Reynolds number using the ADE and MIM models in  
427 the primary fracture.



428

Table 3. Statistical results from the goodness-of-fitting of the ADE and MIM models.

Flow Field no.	$Pe$	$Re$	MIM model		ADE model	
			$R_{MIM}^2$	$E_{MIM}$	$R_{ADE}^2$	$E_{ADE}$
OF#1	8.8	3.1	0.9999	0.0003	0.9992	0.000304
OF#2	81.7	28.5	0.9992	0.0004	0.9994	0.002
OF#3	147.6	51.5	0.9916	0.000927	0.9872	0.002181
OF#4	205.9	71.8	0.9804	0.001285	0.9771	0.002371
PF#1	8.8	3.1	0.9983	0.000707	0.9992	0.000679
PF#2	81.7	28.5	0.9989	0.000224	0.9994	0.000722
PF#3	147.6	51.5	0.9975	0.000361	0.9972	0.001161
PF#4	205.9	71.8	0.9905	0.000529	0.9945	0.001491

429

Table 4. Estimated values of parameters for the MIM and ADE models at different Peclet numbers and Reynolds

430

numbers in both original and primary fractures.

Flow Field no.	$Pe$	$Re$	MIM model				ADE model		
			$\beta$	$\alpha^{*a}$	$\frac{D_{f,MIM}}{D_{Taylor}, (\%_E)^b}$	$\frac{\bar{u}_{f,MIM}}{\bar{u}^c}$	$\frac{D_{f,ADE}}{D_{Taylor}, (\%_E)^b}$	$\frac{\bar{u}_{f,ADE}}{\bar{u}^c}$	
OF#1	8.8	3.1	0.88	3.12	1.26 (26%)	1.03	1.38 (38%)	1.08	
OF#2	81.7	28.5	0.71	4.25	1.17 (17%)	1.05	1.28 (28%)	1.11	
OF#3	147.6	51.5	0.67	3.14	0.92 (8%)	1.09	1.12 (12%)	1.16	
OF#4	205.9	71.8	0.61	5.72	0.81 (19%)	1.12	0.95 (5%)	1.28	
PF#1	8.8	3.1	0.94	5.84	1.11 (11%)	1.02	1.25 (25%)	1.04	
PF#2	81.7	28.5	0.86	6.02	1.01 (1%)	1.02	1.17 (17%)	1.09	
PF#3	147.6	51.5	0.78	4.85	0.98 (2%)	1.03	0.99 (1%)	1.11	
PF#4	205.9	71.8	0.72	6.51	0.92 (8%)	1.05	1.02 (2%)	1.14	

431

<sup>a</sup>  $\alpha^*$  denotes the dimensionless mass transfer coefficient normalized by the characteristic advection time scale,  $\alpha^* =$

432

$\alpha\tau_D = \alpha\bar{b}/\bar{u}$ .

433

<sup>b</sup>  $\%_E$  denotes the percent error between the fitted dispersion and Taylor dispersion.



434 <sup>c</sup>  $\bar{u}$  denotes the mean velocity calculated from the direct simulations.

435

436 The best-fitted velocities of the ADE and MIM models are larger than the mean flow velocity calculated from the  
437 numerical simulations (Table 4). This is mainly due to the fact the transport velocity along the middle of the fractures is  
438 faster than the mean flow velocity. This deviation of the fitted velocity from the mean flow velocity increases as the  
439 Peclet number and Reynolds number increase, since the nonlinear flow behavior (i.e., eddies) increases the variability of  
440 local flow velocity. As expected, the fits of ADE transport velocity to numerical results are better in the primary fracture  
441 than in the original fracture at the same Peclet number and Reynolds number. This indicates that the secondary roughness  
442 enhances the channelling impact on solute transport.

443 For the asymptotic solute transport, the effective dispersion coefficient can be directly predicted by the Taylor  
444 dispersion. For transport through an ideal single fracture with smooth parallel walls, the fluid flow is stratified  
445 (Posieuille), and the Taylor dispersion is defined as,

446

$$D_{Taylor} = \frac{(\bar{u}\bar{b})^2}{210D_m} + D_m = \frac{Q^2}{210D_m} + D_m \quad (27)$$

447 Depending on Eq.(27), we can directly estimate  $D_{Taylor}$  using  $Q$  and  $D_m$  without fitting the BTCs. It should be noted that  
448 the Eq.(27) is only valid for describing solute transport after the asymptotic time and length scale, at which the spreading  
449 of the solute reaches its asymptotic status. This requires that the Peclet number should be less than the critical Peclet  
450 number (Eq. (19)) for a given 2D fracture. Since the Peclet number used in this study is less than the critical Peclet  
451 number, one can expect that the fitted effective dispersion would be equal to the Taylor dispersion in the same fracture



452 with the same Peclet number. Therefore, comparing terms  $D_{f,i}$  and  $D_{Taylor}$  in Table 4 with the same Peclet number in  
453 different fractures can be interpreted as a metric for the influence of roughness on the solute dispersion.

454 Although previous studies (Detwiler et al., 2000; Roux et al., 1998) have shown that the Taylor dispersion was valid  
455 under relatively high Peclet numbers, our results here show that the values of  $D_{f,i}/D_{Taylor}$  are fluctuating around unity,  
456 indicating that the Taylor dispersion either underestimates or overestimates the fitted dispersion from the ADE and MIM  
457 models. This is consistent with previous studies (Wang and Cardenas, 2014), where such a fluctuating difference is  
458 considered as a result of the non-Fickian transport and the influence of fracture heterogeneity and flow inertia forces.  
459 Another observation from Table 4 is that the percent errors between the fitted dispersion and the Taylor dispersion are  
460 much smaller in the primary fracture than in the original fracture. This further indicates that the secondary roughness is a  
461 primary factor that causes the non-Fickian transport.

462 Analyzing the estimated parameters  $\beta$  and  $\alpha^*$  from the MIM model in both the original and primary fractures can  
463 provide insight into the mechanism of the impact of secondary roughness enhancement on non-Fickian transport. The  
464 estimated parameter  $\beta$  decreases while the  $\alpha^*$  generally increases as the Peclet number and Reynolds number increase in  
465 the original and primary fractures, indicating that the immobile domain fraction increases and the mass exchange process  
466 between immobile and mobile domains is enhanced.

467 It is also clearly shown in Figs.4 and 6 that eddies resulting from the nonlinear flow act as an immobile domain and  
468 the mixing and spreading processes of the solute are significantly delayed. An increasing flow velocity results in a higher



469 contact area between the immobile and mobile domains, which in turn gives a rise to the enhanced solute mixing between  
470 these two domains (Cherubini et al., 2014; Gao et al., 2009). As the secondary roughness is removed, the influence of  
471 nonlinear flow characteristics (i.e., eddies and streamline tortuosity) on solute transport is significantly reduced. As a  
472 result, the  $\beta$  value is smaller while the  $\alpha^*$  value is larger in the primary fracture than in the original fracture at the same  
473 Peclet number and Reynolds number.

## 474 6. Summary and Conclusion

475 To investigate the influence of multiscale roughness on the flow and conservative solute transport in the self-affine  
476 fractures, we constructed the self-affine fracture by the SRA and decomposed the original fracture roughness into large-  
477 scale (primary roughness) and small-scale (secondary roughness) roughness. The numerical simulations of flow and  
478 solute transport were conducted in the original fracture and primary fracture (without the secondary roughness) with a  
479 varying range of Peclet number and Reynolds number. This enabled us not only to analyze the flow and solute transport  
480 with consideration of Peclet number and Reynolds number, but also to emphasize the influence of multiscale roughness.

481 The fluid flow was characterized by Forchheimer's law and the results showed that the secondary roughness  
482 significantly enhanced the nonlinear flow (i.e., eddies and tortuous streamlines). Since the simulations of the solute  
483 transport was controlled under the asymptotic transport regime in which the simulated  $Pe$  was less than the critical  $Pe$ ,  
484 any Non-Fickian transport could be considered as a result of fracture roughness rather than the fracture length. BTCs and  
485 RTDs showed that Non-Fickian (i.e., early arrival and long tails) became weak as the Peclet number and Reynolds



486 number increased in both the original and primary fractures. However, it was found that the Non-Fickian behavior was  
487 stronger in the original fracture than in the primary fracture where the secondary roughness was excluded. This indicated  
488 that the secondary roughness significantly enhanced the Non-Fickian transport. A qualitative analysis showed that the  
489 peak concentration in BTCs decreased as the secondary roughness was removed. This implied that the secondary  
490 roughness could be curial for enhancing the solute dilution.

491 It was confirmed through model fitting that the ADE model was incapable of describing the roughness-induced non-  
492 Fickian transport even at the asymptotic time, while the MIM model exhibited better results than the ADE model. The  
493 estimated parameters from these two models showed that due to the influence of channelling flow, the fitted mean  
494 velocity was larger than the mean flow velocity from the numerical simulations. After removing the secondary roughness,  
495 we found that the deviation of the fitted velocity from the mean flow velocity was decreased. The mobile domain fraction  
496 decreased while the mass exchange rate generally increased between the immobile and mobile domains as the Peclet  
497 number and Reynolds number increased. The secondary roughness resulted in the decreasing mobile domain fraction and  
498 the increasing mass exchange rate.

499 Our study provides insight into the influence of multiscale roughness on flow and solute transport behavior in  
500 fractures. The current works and the idea of decomposing the fracture roughness into two different scales may also be  
501 important to upscale roughness-induced non-Fickian transport. Further investigation is needed to extend this study to  
502 conservative and reactive solute transport with the consideration of three-dimensional fractures and the pre-asymptotic  
503 time scale.



## 504 **Acknowledgement**

505 The work is supported by the National Natural Science Foundation of China (Nos.41602239 and 41572209), the  
506 Fundamental Research Funds of the Central Universities (No.2016B05514), the International Postdoctoral Exchange  
507 Fellowship Program (No.20150048) and the Natural Science Foundation of Jiangsu Province (No.SBK20160861).

## 508 **References**

- 509 Aris, R.: On the Dispersion of a Solute in a Fluid Flowing through a Tube, Proceedings of the Royal Society of London A:  
510 Mathematical, Physical and Engineering Sciences, 235, 67-77, 10.1098/rspa.1956.0065, 1956.
- 511 Barton, N.: Suggested methods for the quantitative description of discontinuities in rock masses, ISRM, International Journal of  
512 Rock Mechanics and Mining Sciences & Geomechanics Abstracts, 15, 1978.
- 513 Bauguet, F., and Fourar, M.: Non-Fickian dispersion in a single fracture, Journal of Contaminant Hydrology, 100, 137-148,  
514 <http://dx.doi.org/10.1016/j.jconhyd.2008.06.005>, 2008.
- 515 Bear, J.: Dynamics of fluids in porous materials, Society of Petroleum Engineers, 1972.
- 516 Becker, M. W., and Shapiro, A. M.: Interpreting tracer breakthrough tailing from different forced - gradient tracer experiment  
517 configurations in fractured bedrock, Water Resources Research, 39, 2003.
- 518 Benson, D. A.: The Fractional Advection--Dispersion Equation: Development and Application, University of Nevada Reno, 1998.
- 519 Berkowitz, B.: Characterizing flow and transport in fractured geological media: A review, Advances in Water Resources, 25, 861-  
520 884, [http://dx.doi.org/10.1016/S0309-1708\(02\)00042-8](http://dx.doi.org/10.1016/S0309-1708(02)00042-8), 2002.
- 521 Berkowitz, B., Cortis, A., Dentz, M., and Scher, H.: Modeling non-Fickian transport in geological formations as a continuous time  
522 random walk, Reviews of Geophysics, 44, 10.1029/2005rg000178, 2006.
- 523 Bijeljic, B., and Blunt, M. J.: Pore-scale modeling and continuous time random walk analysis of dispersion in porous media, Water  
524 Resources Research, 42, n/a-n/a, 10.1029/2005WR004578, 2006.
- 525 Boffa, J., Allain, C., and Hulin, J.: Experimental analysis of fracture rugosity in granular and compact rocks, The European Physical  
526 Journal-Applied Physics, 2, 281-289, 1998.
- 527 Bouquain, J., Méheust, Y., Bolster, D., and Davy, P.: The impact of inertial effects on solute dispersion in a channel with periodically  
528 varying aperture, Physics of Fluids, 24, 083602, 10.1063/1.4747458, 2012.
- 529 Boutt, D. F., Grasselli, G., Fredrich, J. T., Cook, B. K., and Williams, J. R.: Trapping zones: The effect of fracture roughness on the  
530 directional anisotropy of fluid flow and colloid transport in a single fracture, Geophysical Research Letters, 33, n/a-n/a,  
531 10.1029/2006GL027275, 2006.



- 532 Briggs, S., Karney, B. W., and Sleep, B. E.: Numerical modelling of flow and transport in rough fractures, *Journal of Rock Mechanics*  
533 *and Geotechnical Engineering*, 6, 535-545, <http://dx.doi.org/10.1016/j.jrmge.2014.10.004>, 2014.
- 534 Briggs, S., Karney, B. W., and Sleep, B. E.: Numerical modeling of the effects of roughness on flow and eddy formation in fractures,  
535 *Journal of Rock Mechanics and Geotechnical Engineering*, <http://dx.doi.org/10.1016/j.jrmge.2016.08.004>, 2016.
- 536 Brown, S. R.: Fluid flow through rock joints: The effect of surface roughness, *Journal of Geophysical Research: Solid Earth*, 92, 1337-  
537 1347, 10.1029/JB092iB02p01337, 1987.
- 538 Brush, D. J., and Thomson, N. R.: Fluid flow in synthetic rough-walled fractures: Navier-Stokes, Stokes, and local cubic law  
539 simulations, *Water Resources Research*, 39, n/a-n/a, 10.1029/2002wr001346, 2003.
- 540 Cardenas, M. B., Slottke, D. T., Ketcham, R. A., and Sharp, J. M.: Navier - Stokes flow and transport simulations using real fractures  
541 shows heavy tailing due to eddies, *Geophysical Research Letters*, 34, 2007.
- 542 Cherubini, C., Giasi, C. I., and Pastore, N.: On the reliability of analytical models to predict solute transport in a fracture network,  
543 *Hydrology and Earth System Sciences*, 18, 2359, 2014.
- 544 Dentz, M., and Berkowitz, B.: Transport behavior of a passive solute in continuous time random walks and multirate mass transfer,  
545 *Water Resources Research*, 39, n/a-n/a, 10.1029/2001WR001163, 2003.
- 546 Dentz, M., Cortis, A., Scher, H., and Berkowitz, B.: Time behavior of solute transport in heterogeneous media: transition from  
547 anomalous to normal transport, *Advances in Water Resources*, 27, 155-173, <http://dx.doi.org/10.1016/j.advwatres.2003.11.002>,  
548 2004.
- 549 Dentz, M., Le Borgne, T., Englert, A., and Bijeljic, B.: Mixing, spreading and reaction in heterogeneous media: A brief review, *Journal*  
550 *of Contaminant Hydrology*, 120–121, 1-17, <http://dx.doi.org/10.1016/j.jconhyd.2010.05.002>, 2011.
- 551 Detwiler, R. L., Rajaram, H., and Glass, R. J.: Solute transport in variable-aperture fractures: An investigation of the relative  
552 importance of Taylor dispersion and macrodispersion, *Water Resources Research*, 36, 1611-1625, 2000.
- 553 Dou, Z., Zhou, Z., and Sleep, B. E.: Influence of wettability on interfacial area during immiscible liquid invasion into a 3D self-affine  
554 rough fracture: Lattice Boltzmann simulations, *Advances in Water Resources*, 61, 1-11,  
555 <http://dx.doi.org/10.1016/j.advwatres.2013.08.007>, 2013.
- 556 Dou, Z., and Zhou, Z.-f.: Lattice Boltzmann simulation of solute transport in a single rough fracture, *Water Science and Engineering*,  
557 7, 277-287, 2014.
- 558 Dou, Z., Chen, Z., Zhou, Z., Wang, J., and Huang, Y.: Influence of eddies on conservative solute transport through a 2D single self-  
559 affine fracture, *International Journal of Heat and Mass Transfer*, 121, 597-606,  
560 <https://doi.org/10.1016/j.ijheatmasstransfer.2018.01.037>, 2018a.
- 561 Dou, Z., Zhou, Z., Wang, J., and Huang, Y.: Roughness scale dependence of the relationship between tracer longitudinal dispersion  
562 and Peclet number in variable - aperture fractures, *Hydrological Processes*, 32, 1461-1475, doi:10.1002/hyp.11505, 2018b.
- 563 Drazer, G., Auradou, H., Koplik, J., and Hulin, J.: Self-affine fronts in self-affine fractures: Large and small-scale structure, *Physical*  
564 *review letters*, 92, 014501, 2004.
- 565 Dreuzy, J.-R. d., and Carrera, J.: On the validity of effective formulations for transport through heterogeneous porous media,  
566 *Hydrology and Earth System Sciences*, 20, 1319-1330, 2016.
- 567 Dreuzy, J. R., Carrera, J., Dentz, M., and Le Borgne, T.: Time evolution of mixing in heterogeneous porous media, *Water Resources*  
568 *Research*, 48, n/a-n/a, 10.1029/2011WR011360, 2012.



- 569 Fetter, C. W.: Applied hydrogeology, Prentice hall, 2000.
- 570 Fiori, A., and Becker, M. W.: Power law breakthrough curve tailing in a fracture: The role of advection, *Journal of Hydrology*, 525,  
571 706-710, <https://doi.org/10.1016/j.jhydrol.2015.04.029>, 2015.
- 572 Gao, G., Zhan, H., Feng, S., Huang, G., and Mao, X.: Comparison of alternative models for simulating anomalous solute transport in  
573 a large heterogeneous soil column, *Journal of Hydrology*, 377, 391-404, <http://dx.doi.org/10.1016/j.jhydrol.2009.08.036>, 2009.
- 574 Haggerty, R.: Analytical solution and simplified analysis of coupled parent - daughter steady - state transport with multirate mass  
575 transfer, *Water Resources Research*, 49, 635-639, 2013.
- 576 Jacob, B.: Dynamics of fluids in porous media, New York, 1972.
- 577 Javadi, M., Sharifzadeh, M., Shahriar, K., and Mitani, Y.: Critical Reynolds number for nonlinear flow through rough-walled  
578 fractures: The role of shear processes, *Water Resources Research*, 50, 1789-1804, [10.1002/2013WR014610](https://doi.org/10.1002/2013WR014610), 2014.
- 579 Jiménez - Hornero, F., Giráldez, J., Laguna, A., and Pachepsky, Y.: Continuous time random walks for analyzing the transport of a  
580 passive tracer in a single fissure, *Water resources research*, 41, 2005.
- 581 Jin, Y., Dong, J., Zhang, X., Li, X., and Wu, Y.: Scale and size effects on fluid flow through self-affine rough fractures, *International*  
582 *Journal of Heat and Mass Transfer*, 105, 443-451, <http://dx.doi.org/10.1016/j.ijheatmasstransfer.2016.10.010>, 2017.
- 583 Kang, P. K., Brown, S., and Juanes, R.: Emergence of anomalous transport in stressed rough fractures, *Earth and Planetary Science*  
584 *Letters*, 454, 46-54, <http://dx.doi.org/10.1016/j.epsl.2016.08.033>, 2016.
- 585 Kitanidis, P. K.: The concept of the Dilution Index, *Water Resources Research*, 30, 2011-2026, [10.1029/94WR00762](https://doi.org/10.1029/94WR00762), 1994.
- 586 Konzuk, J. S., and Kueper, B. H.: Evaluation of cubic law based models describing single-phase flow through a rough-walled fracture,  
587 *Water Resources Research*, 40, n/a-n/a, [10.1029/2003WR002356](https://doi.org/10.1029/2003WR002356), 2004.
- 588 Le Borgne, T., Dentz, M., Bolster, D., Carrera, J., de Dreuzy, J.-R., and Davy, P.: Non-Fickian mixing: Temporal evolution of the scalar  
589 dissipation rate in heterogeneous porous media, *Advances in Water Resources*, 33, 1468-1475,  
590 <http://dx.doi.org/10.1016/j.advwatres.2010.08.006>, 2010.
- 591 Lee, S. H., Yeo, I. W., Lee, K.-K., and Detwiler, R. L.: Tail shortening with developing eddies in a rough-walled rock fracture,  
592 *Geophysical Research Letters*, 42, 6340-6347, [10.1002/2015GL065116](https://doi.org/10.1002/2015GL065116), 2015.
- 593 Mallat, S. G.: A theory for multiresolution signal decomposition: the wavelet representation, *IEEE transactions on pattern analysis*  
594 *and machine intelligence*, 11, 674-693, 1989.
- 595 Mandelbrot, B. B.: The fractal geometry of nature, Macmillan, 1983.
- 596 Neuman, S. P., and Tartakovsky, D. M.: Perspective on theories of non-Fickian transport in heterogeneous media, *Advances in*  
597 *Water Resources*, 32, 670-680, 2009.
- 598 Nowamooz, A., Radilla, G., Fourar, M., and Berkowitz, B.: Non-Fickian transport in transparent replicas of rough-walled rock  
599 fractures, *Transport in porous media*, 98, 651-682, 2013.
- 600 Oron, A. P., and Berkowitz, B.: Flow in rock fractures: The local cubic law assumption reexamined, *Water Resources Research*, 34,  
601 2811-2825, [10.1029/98WR02285](https://doi.org/10.1029/98WR02285), 1998.
- 602 Qian, J., Chen, Z., Zhan, H. B., and Luo, S. H.: Solute transport in a filled single fracture under non-Darcian flow, *International*  
603 *Journal of Rock Mechanics and Mining Sciences*, 48, 132-140, <https://doi.org/10.1016/j.ijrmms.2010.09.009>, 2011a.
- 604 Qian, J., Zhan, H., Chen, Z., and Ye, H.: Experimental study of solute transport under non-Darcian flow in a single fracture, *Journal*  
605 *of Hydrology*, 399, 246-254, <http://dx.doi.org/10.1016/j.jhydrol.2011.01.003>, 2011b.



- 606 Qian, J., Liang, M., Chen, Z., and Zhan, H.: Eddy correlations for water flow in a single fracture with abruptly changing aperture,  
607 Hydrological Processes, 26, 3369-3377, 10.1002/hyp.8332, 2012.
- 608 Renshaw, C. E.: On the relationship between mechanical and hydraulic apertures in rough - walled fractures, Journal of  
609 Geophysical Research: Solid Earth, 100, 24629-24636, 1995.
- 610 Roux, S., Plouraboué, F., and Hulin, J.-P.: Tracer Dispersion in Rough Open Cracks, Transport in Porous Media, 32, 97-116,  
611 10.1023/a:1006553902753, 1998.
- 612 Schmittbuhl, J., Gentier, S., and Roux, S.: Field measurements of the roughness of fault surfaces, Geophysical Research Letters, 20,  
613 639-641, 1993.
- 614 Thompson, M. E.: Numerical simulation of solute transport in rough fractures, Journal of Geophysical Research: Solid Earth, 96,  
615 4157-4166, 10.1029/90JB02385, 1991.
- 616 Toride, N., Leij, F., and Van Genuchten, M. T.: The CXTFIT code for estimating transport parameters from laboratory or field tracer  
617 experiments, 1, version, 1995.
- 618 Tsang, Y. W., and Tsang, C. F.: Flow channeling in a single fracture as a two-dimensional strongly heterogeneous permeable  
619 medium, Water Resources Research, 25, 2076-2080, 10.1029/WR025i009p02076, 1989.
- 620 Van Genuchten, M. T., and Wierenga, P.: Mass transfer studies in sorbing porous media I. Analytical solutions, Soil Science Society  
621 of America Journal, 40, 473-480, 1976.
- 622 Voss, R. F.: Fractals in nature: from characterization to simulation, in: The science of fractal images, Springer, 21-70, 1988.
- 623 Wang, L., Cardenas, M. B., Deng, W., and Bennett, P. C.: Theory for dynamic longitudinal dispersion in fractures and rivers with  
624 Poiseuille flow, Geophysical Research Letters, 39, 2012.
- 625 Wang, L., and Cardenas, M. B.: Non - Fickian transport through two - dimensional rough fractures: Assessment and prediction,  
626 Water Resources Research, 50, 871-884, 2014.
- 627 Wang, L., and Cardenas, M. B.: An efficient quasi-3D particle tracking-based approach for transport through fractures with  
628 application to dynamic dispersion calculation, Journal of Contaminant Hydrology, 179, 47-54,  
629 <http://dx.doi.org/10.1016/j.jconhyd.2015.05.007>, 2015.
- 630 Wang, L., Cardenas, M. B., Slottke, D. T., Ketcham, R. A., and Sharp, J. M.: Modification of the Local Cubic Law of fracture flow for  
631 weak inertia, tortuosity, and roughness, Water Resources Research, 51, 2064-2080, 2015.
- 632 Wang, L., and Cardenas, M. B.: Transition from non-Fickian to Fickian longitudinal transport through 3-D rough fractures: Scale-  
633 (in)sensitivity and roughness dependence, Journal of Contaminant Hydrology, 198, 1-10,  
634 <https://doi.org/10.1016/j.jconhyd.2017.02.002>, 2017.
- 635 Wang, M., Chen, Y.-F., Ma, G.-W., Zhou, J.-Q., and Zhou, C.-B.: Influence of surface roughness on nonlinear flow behaviors in 3D  
636 self-affine rough fractures: Lattice Boltzmann simulations, Advances in Water Resources, 96, 373-388,  
637 <http://dx.doi.org/10.1016/j.advwatres.2016.08.006>, 2016.
- 638 Zheng, Q., Dickson, S., and Guo, Y.: Influence of aperture field heterogeneity and anisotropy on dispersion regimes and dispersivity  
639 in single fractures, Journal of Geophysical Research: Solid Earth, 114, 10.1029/2007JB005161, 2009.
- 640 Zhou, J.-Q., Hu, S.-H., Fang, S., Chen, Y.-F., and Zhou, C.-B.: Nonlinear flow behavior at low Reynolds numbers through rough-walled  
641 fractures subjected to normal compressive loading, International Journal of Rock Mechanics and Mining Sciences, 80, 202-218,  
642 <http://dx.doi.org/10.1016/j.ijrmms.2015.09.027>, 2015.



643 Zimmerman, R., Kumar, S., and Bodvarsson, G.: Lubrication theory analysis of the permeability of rough-walled fractures,  
644 International Journal of Rock Mechanics and Mining Sciences & Geomechanics Abstracts, 1991, 325-331,  
645 Zimmerman, R. W., and Bodvarsson, G. S.: Hydraulic conductivity of rock fractures, Transport in porous media, 23, 1-30, 1996.  
646 Zou, L., Jing, L., and Cvetkovic, V.: Roughness decomposition and nonlinear fluid flow in a single rock fracture, International Journal  
647 of Rock Mechanics and Mining Sciences, 75, 102-118, <http://dx.doi.org/10.1016/j.ijrmms.2015.01.016>, 2015.

648